Coastal upwelling events, salinity stratification, and barrier layer observed along the southwestern coast of Sumatra

T. Horii[1], I. Ueki[1], and K. Ando[1]

[1]Research Institute for Global Change, Japan Agency for Marine-Earth Science and Technology, 2-15, Natsushima, Yokosuka, Kanagawa 237-0061 Japan.

Corresponding author: Takanori Horii (horiit@jamstec.go.jp)

Horii Takanori(ORCID ID: 0000-0003-2044-4226)

Ueki Iwao (ORCID ID: 0000-0002-8760-2666)

Ando Kentaro (ORCID ID: 0000-0003-1924-3910)

Key Points:

- Coastal upwelling along the southwestern coast of Sumatra was observed by two Argo floats
- Prominent features of the coastal upwelling system were salinity stratification and a thick barrier layer related to local precipitation
- We suggest that the ocean vertical structure is unfavorable for subsurface upwelling signals to appear in the surface layer

Abstract

Coastal upwelling along the southwestern coast of Sumatra is a seasonal upwelling that occurs in areas of high sea surface temperature and abundant precipitation at the southeastern edge of the Indian Ocean warm pool. Based on observations from two Argo floats that drifted and stayed around Sumatra, we investigated ocean temperature and salinity variations during several coastal upwelling events observed in 2013–2017. The Argo floats observed the vertical structure of temperature and salinity every 10 days within 100 km from the southwestern coast of Sumatra. The observation data show intraseasonal-scale subsurface temperature cooling events with significant upward displacements of the thermocline and high-salinity water, led by anomalous local southwesterly winds and equatorial easterly winds. During the coastal upwelling events, salinity stratification and a thick barrier layer related to local precipitation were also observed. Surface mixed layer temperature cooling were relatively small in contrast to the significant subsurface anomalies. It was found that during the coastal upwelling events, subsurface cold-water upwelling signals did not necessarily reach the mixed layer when salinity stratification and a thick barrier layer were present. The implications of these observational results for understanding the local atmosphere ocean interaction, and hence the occurrence of the Indian Ocean Dipole, are discussed.

Plain Language Summary

Coastal upwelling is an important phenomenon in the ocean that provides nutrient-rich water from several tens of meters below the sea surface as well as abundant fishing grounds. The area southwest of Sumatra island is one of the regions where coastal upwelling are observed from June to September. Regarding the coastal upwelling, there have been no observational studies for ocean variations below the sea surface. We used data from ocean observation floats called “Argo floats.” These floats remained near the coastal region and observed coastal upwelling signals from the sea surface down to several hundreds of meters. The data demonstrates that the temperature and salinity variations during the coastal upwelling are unique, because the signals were often controlled by a dramatic difference in water density between the surface low-salinity water and the high-salinity water below. The data suggest that the cold-water upwelling signals are less likely to appear at the sea surface due to the large vertical salinity changes, probably because this layer limits the connection between subsurface cold water and surface warm water. This finding will help to clarify the variability of ocean temperature in the eastern Indian Ocean and to better estimate heat exchange between ocean and atmosphere.

1 Introduction

Coastal upwelling in the ocean is caused by alongshore wind forcing, resultant offshore Ekman mass transport, and cold-water upwelling with a spatial scale of several tens to several hundreds of kilometers from the coast (Charney, 1955; Yoshida, 1955). During a coastal upwelling event, cold and nutrient-rich water is brought upward, reaches the ocean mixed layer, and influences the ocean surface heat balance, the biogeochemical balance, and coastal ecosystems that host regional fisheries. One such monsoon-induced seasonal upwelling system is that along the southwestern coasts of Sumatra and Java in the eastern Indian Ocean (Wyrtki, 1962).

The eastern tropical Indian Ocean is characterized by high average sea surface temperature (SST), abundant precipitation around the Maritime Continent (e.g., Mori et al., 2004), active intraseasonal variation (Zhang, 2005 for a review), and year-to-year SST variation represented by the Indian Ocean Dipole (IOD) phenomenon (Saji et al., 1999). Along the coasts of Sumatra and Java, coastal upwelling develops mainly in June–September (Wyrtki, 1962; Bray et al., 1996; Susanto et al., 2001; Du et al., 2005). This upwelling helps to develop the IOD (e.g., Du et al., 2008; Chen et al., 2016; Delman et al., 2016; 2018) because it provides cold water that subsequently cools the eastern tropical Indian Ocean (e.g., Murtugudde et al., 2000; Halkides and Lee, 2009). Interannual variability of ocean subsurface temperature related to upwelling off Sumatra is robust enough to be detected from coral-based reconstructed ocean temperature data collected over a long period of 1943-1992 (Grumet et al., 2004). During the IOD, cold SST anomalies are centered around 5°S off Sumatra (e.g., Horii et al., 2009; Kämpf and Kavi, 2019). Considering that the anomalous equatorial zonal SST gradient is a pivotal condition of the IOD (Saji et al., 1999; Webster et al., 1999), cold-water advection from upwelling southwest of Sumatra plays a crucial role in the IOD development.

Past studies have investigated the coastal upwelling along the coasts of Sumatra and Java as an upwelling system at the eastern boundary of the tropical Indian Ocean (Susanto et al., 2001; Halkides and Lee, 2009). The coastal upwelling signals, which are highly correlated with the El Niño/Southern Oscillation (ENSO) and the IOD (Susanto et al., 2001), appear as a continuous signal along the coasts of Sumatra, Java, Bali, and further east to the Lesser Sunda Islands (Susanto and Marra, 2005; Ningsih et al., 2013). However, climatological SST variation related to the Sumatra and Java upwelling system differs significantly (Figure 1). The seasonal upwelling signal southwest of Sumatra is smaller than that south of Java, such that climatological SST variation is less than half as compared to that south of Java. Using a linear two-layer model, Kämpf and Kavi (2019) explained why coastal upwelling was stronger south of Java than southwest of Sumatra. Another difference is the surface salinity, because abundant precipitation is more concentrated around Sumatra than around Java (Aldrian and Susanto, 2003; As-Syakur et al., 2016). Given these references, the ocean vertical structure southwest of Sumatra must be studied as a distinct upwelling system in the eastern Indian Ocean.

Past studies presented the coastal upwelling signal mainly using satellite-based observations or limited timeseries. Thus, the ocean vertical structure southwest of Sumatra has not been much reported. For example, Susanto et al. (2001) and Susanto and Marra (2005) used satellite-based observations to observe the coastal upwelling, focusing only on SST and/or Chlorophyll-a variations at the sea surface. Qu and Meyers (2005) used historical hydrographic data and investigated seasonal temperature and salinity variations in the southeast Indian Ocean, but they mainly presented mixed layer and barrier layer variations in the open ocean. Susanto et al. (2016) presented ocean vertical profiles of temperature, salinity, and currents from conductivity-temperature-depth (CTD) casts in the Sunda Strait (around 105°E–106°E, 6.6°S–5.8°S), but they focused on water properties in terms of the Indonesian Throughflow (ITF). Moteki et al. (2018) used CTD observation obtained by Research Vessel Mirai stationed approximately 50 km off the southwestern coast of Sumatra (4°S, 102°E) and presented the ocean vertical structure during the period of from late-November to mid-December 2015. Although they reported salinity stratification, barrier layer, and their dramatic temporal variation, their results were based on short timeseries of less than one month and not during a season of coastal upwelling. Using the Ocean General Circulation Model for the Earth Simulator (OFES) (Masumoto et al., 2004), Du et al. (2005) and Du et al. (2008) investigated mean seasonal cycle

and its interannual variability off Sumatra and Java. They reported heat budgets and seasonal variation in the coastal upwelling with a monthly time scale. However, the vertical density structure for the coastal region was less produced in the OFES or data assimilation product in terms of intraseasonal time scale (Moteki et al., 2018). The reason for the reduced reproducibility in the models is due to fewer observation data and complicated density variability with frequent freshwater input. Thus, the actual amplitude, the temperature and density structure, and the temporal evolution of the coastal upwelling southwest of Sumatra are not well understood.

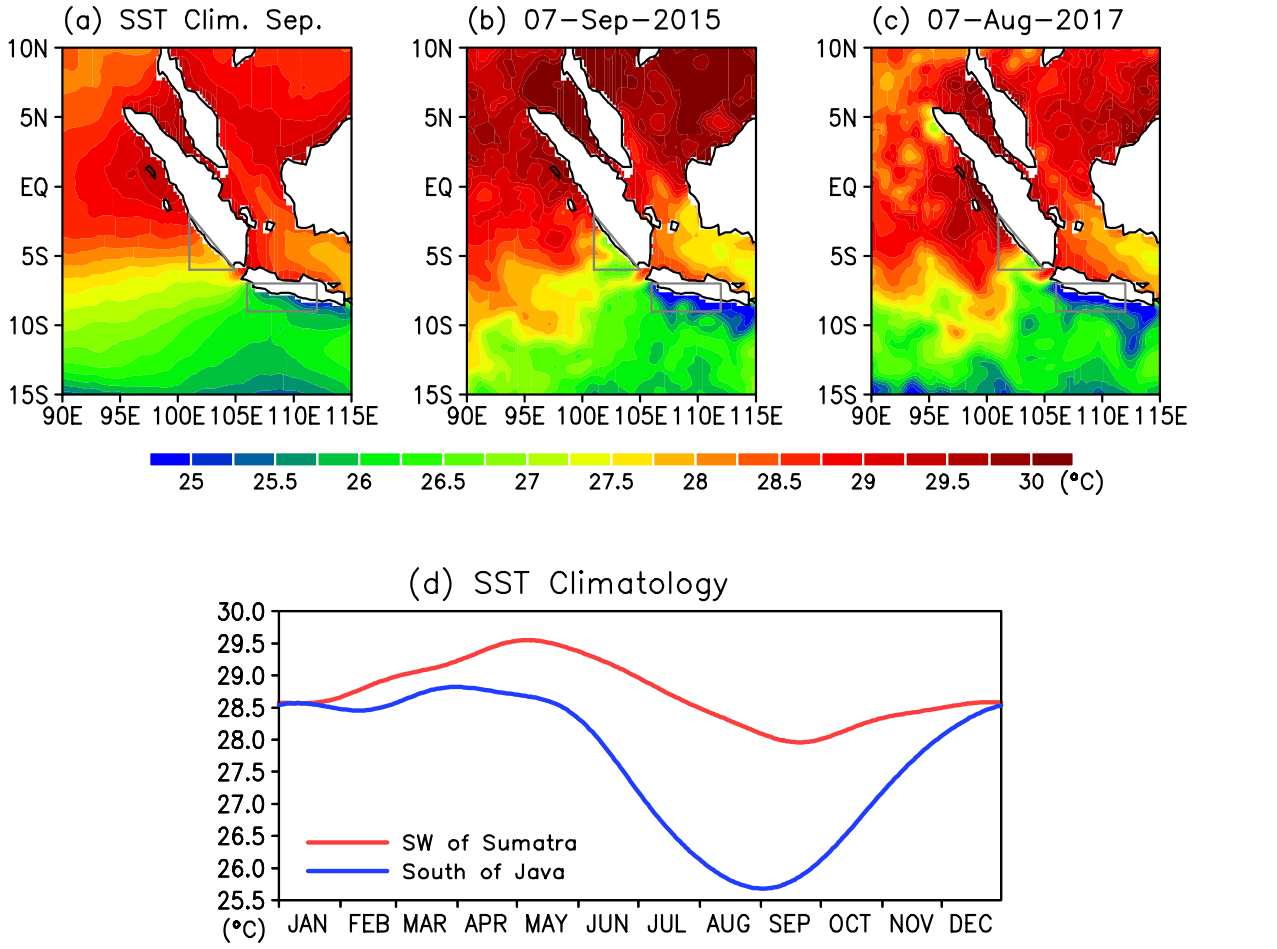

Figure 1. (a) Climatological mean sea surface temperature (SST) in September, based on the data from 1982 to 2011. (b) SST snapshot on 7 September, 2015. (c) As in (b), but on 7 August, 2017. (d) Timeseries of SST averaged for the southwest of Sumatra (red: 101°E–105°E, 6°S–2°S) and for the south of Java (blue: 106°E–112°E, 9°S–7°S).

Based on timeseries obtained by an Argo float that remained south of Java (< 100 km from the coast) approximately half a year, Horii et al. (2018) demonstrated temperature and salinity variations during intraseasonal-scale coastal upwelling events with fine vertical resolution. They reported that thermocline variation during an intraseasonal upwelling event can be approximated by a linear two-layer model, in line with traditional coastal upwelling theory (e.g., Yoshida, 1955). They also demonstrated that the upwelling events were associated with the easterly phase (or 'dry phase') of atmospheric intraseasonal variation in the tropical Indian Ocean (e.g., Madden and Julian, 1994; Lawrence and Webster, 2002). Southwest of Sumatra, because of the lower latitudes (approximately 4°S) compared to those of Java (approximately 8°S–9°S), we expect a larger spatial scale and stronger impact from equatorial Kelvin waves on the upwelling system. The constant density stratification and complicated vertical structure due to the large freshwater input (Moteki et al., 2018) should be elucidated using a longer timeseries in order to understand intraseasonal, seasonal, and year-to-year variations of the coastal upwelling system. In particular, we focus on the possible process by which the previously reported upper ocean stratification (e.g., Du et al., 2005) affects the mixed layer heat balance off Sumatra through changing ocean vertical process. In the present study, using timeseries from available Argo floats that remained in the coastal region southwest of Sumatra, we investigate the vertical structure and its temporal variation associated with the coastal upwelling.

The remainder of this paper is organized as follows. In Section 2, we present details of the observation data and data processing procedures. Section 3 describes the observed features of several coastal upwelling events southwest of Sumatra. Section 4 examines the local wind and freshwater forcing during the coastal upwelling events associated with large-scale atmospheric variation. The results and implications are discussed and summarized in Section 5 and 6.

2 Data and processing

We used the temperature and salinity profiles of two Argo floats southwest of Sumatra obtained from the Advanced automatic QC (AQC) Argo Data by JAMSTEC (http://www.jamstec.go.jp/ARGO/argo_web/argo/?lang=en). One of the Argo floats (WMO number: 2901092) used was originally deployed in the equatorial Indian Ocean in January 2009. This float approached Sumatra in February–March 2013 and reported ocean profiles southwest of Sumatra until 28 October 2013 (Figure 2a). The other (WMO number: 5903908) was also originally deployed in the open ocean (south equatorial Indian Ocean) in November 2011. This float drifted to Sumatra in September 2015, remained there for approximately two years until September 2017, and then floated away to the open ocean (Figure 2b). These Argo floats measured temperature and salinity every 10 days. After estimating the spatial scale of the coastal upwelling, we focused on the data within 100 km from Sumatra coast. (See Section 3 for details.) The distance to the Sumatra coast was estimated based on bathymetry data of the Shuttle Radar Topography Mission (SRTM) 15+ at 15 arc seconds (Tozer et al., 2019). After checking the QC flag of each profile, we used the data for 0–300 dbar in 2013 (number: 2901092) and 2015–2017 (number: 5903908).

We interpolated the temperature and salinity profiles vertically to every 1 m using the Akima spline method (Akima, 1970). Because more than 30% of the data above 6 dbar were missing values, we used the values at 6 dbar as the surface. For these ocean profiles, isothermal layer depth (ILD) was defined using temperature difference ($\Delta T = 0.5°C$) from the surface. The mixed layer depth (MLD) was estimated using the density difference ($\Delta\sigma_\theta = 0.125$ kg m^3) from

the surface. The layer between the MLD and the ILD was defined as the barrier layer (Lukas and Lindstrom, 1991; Sprintall and Tomczak, 1992). We also evaluated the MLD using other density criteria such as that equivalent to an ocean temperature change of 0.5°C from the surface (Sprintall and Tomczak, 1992), and the results were almost identical.

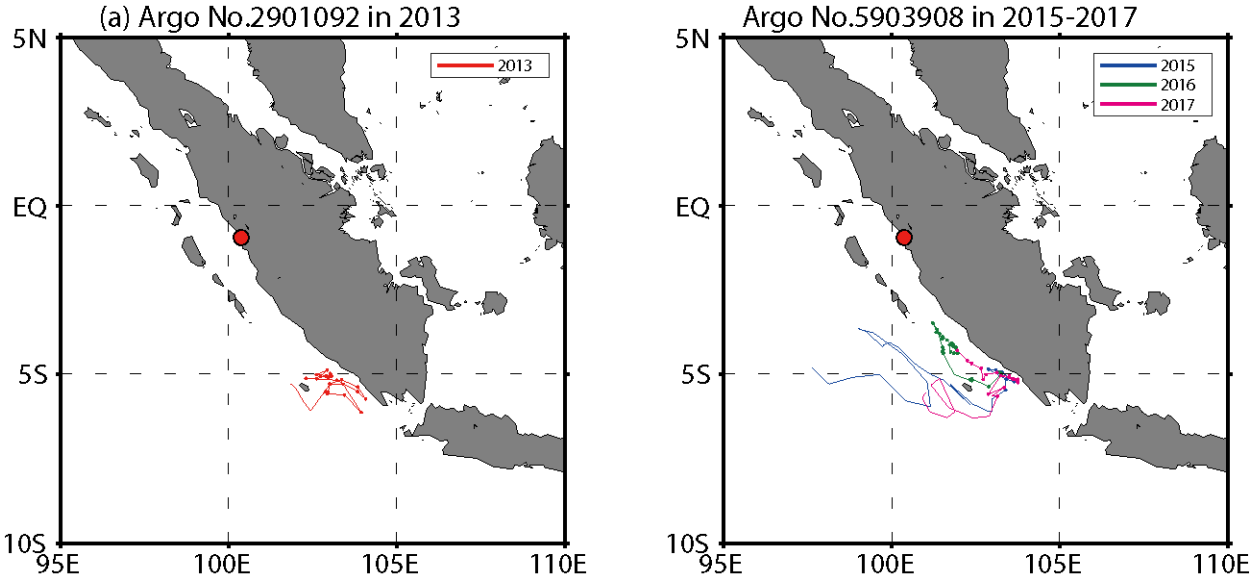

Figure 2. Trajectories (observation points) of the two Argo floats. (a) Argo No. 2901092 in 2013 (red). (b) Argo No. 5903908 in 2015 (blue), 2016 (green), and 2017 (magenta). Small dots indicate observations less than 100 km from the coast of Sumatra. The red circle at 0.95°S, 100.37°E indicates the location of the Indonesian tidal station (Padang).

To observe the coastal upwelling signals southwest of Sumatra, we also used hourly sea level data from an Indonesian tidal station: Padang (0.95°S, 100.37°E, Figure 2). We obtained the quality-checked data from the website of the University of Hawaii Sea Level Center (UHSLC) (Caldwell et al., 2015; available from http://uhslc.soest.hawaii.edu). We prepared a daily sea level anomaly (SLA) timeseries with the following procedure. First, barometric effects were corrected by subtracting sea level pressure data obtained from the National Centers for Environmental Prediction (NCEP)/National Center for Atmospheric Research (NCAR) reanalysis dataset (Kalnay et al., 1996). Then, the timeseries of the SLA during 2012-2018 was calculated from the temporal mean of the timeseries. We applied a 48-hour tide killer filter (Hanawa and Mitsudera, 1985) to remove the high-frequency variability associated with semidiurnal and diurnal tides. Finally, we averaged the hourly data to obtain daily data. For more information on the data processing of the sea level data, see Horii et al. (2016).

We used satellite-based datasets to examine local and large-scale atmospheric and oceanic variations related to the coastal upwelling. Sea surface temperature (SST) data was obtained from the National Oceanic and Atmospheric Administration (NOAA) daily optimum interpolation (OI) SST version-2 dataset on a 0.25° × 0.25° grid (Reynolds et al., 2007). Gridded SLA data (Global Ocean Gridded L4 Sea Surface Heights and Derived Variables Near Real Time) was obtained from Copernicus–Marine Environment Monitoring Service (http://marine.copernicus.eu/). The timeseries of the Indian Ocean dipole mode index (DMI) was

calculated using the OI SST. The DMI is defined as the difference in the SST anomalies between the western (50°E–70°E, 10°S–10°N) and eastern parts (90°E–110°E, 10°S–0°) of the tropical Indian Ocean (Saji et al., 1999). Daily sea surface wind dataset on 0.25° × 0.25° grid was obtained from the Advanced Scatterometer (ASCAT) level-3 product (Bentamy and Fillon, 2012) through Asia-Pacific Data-Research Center (APDRC; http://apdrc.soest.hawaii.edu/). A daily rainfall dataset on a 0.25° × 0.25° grid was obtained from the Precipitation Estimation from Remotely Sensed Information using Artificial Neural Networks (PERSIANN) - Climate Data Record (CDR) product (Nguyen et al., 2019) by the Center for Hydrometeorology and Remote Sensing (CHRS, https://chrsdata.eng.uci.edu/). A daily outgoing longwave radiation (OLR) dataset was obtained from the NCAR/NOAA interpolated dataset (Liebmann and Smith, 1996). To remove shorter time scales of less than a few days, all data except for Argo data were smoothed with a 5-day running mean filter.

When we observed intraseasonal-scale variation, we used a Lanczos band-pass filter with 20-day and 50-day cutoff periods. We set the cutoff periods based on a spectrum analysis of sea level variations related to coastal upwelling signals at the southwestern coast of Sumatra (Horii et al., 2016). We confirmed that minor modifications of the cut-off frequency did not lead to fundamentally different conclusions of the present study.

3 Observed coastal upwelling events

3.1. Definition

Argo floats observed the seasonal and year-to-year variations of temperature and salinity near the southwestern coast of Sumatra in 2013 and 2015–2017 (Figure 3). On the intraseasonal to seasonal time scale, the observed thermocline variation was roughly in inverse phase with the sea level variation at Sumatra (0.95°S, 100.37°E; Figure 2), indicating that Argo observation, even for a resolution of 10 days, could capture coastal upwelling signals.

Based on the data of the Argo floats and using the definition described below, we focused on 12 intraseasonal-scale coastal upwelling events. First, we estimated the spatial scale of coastal upwelling along the southwestern coast of Sumatra as the first internal radius of deformation $(g' H)^{1/2}/f$, where g' is the reduced gravity, H is the upper-layer thickness, and f is the Coriolis parameter (Yoshida, 1955). We focused on the months from May to October, in which typical intraseasonal-scale upwelling events with anomalous southeasterly winds were observed. We computed g' and H from 57 density profiles of the Argo floats in 2013 and 2015–2017, and estimated $(g' H)^{1/2}$ to be 1.17 to 3.32 m s^{-1}. The estimate of the phase speed of the first baroclinic mode $(g' H)^{1/2}$ is consistent with a previous study (Matsuyama et al., 1996). According to the average observation points of coastal upwelling peaks (4.98°S, 102.91°E), f was set to be 1.017×10^{-5} s^{-1}, which yielded a horizontal scale of 92 to 261 km. As a practical estimate, we set the threshold for the observation data of 100 km from the coast. Then, we observed temperature profiles in which the upper thermocline (25°C isotherm) was shallower than 100 m when the distance to Sumatra was within 100 km (Figures 3b and 3f). We set a peak of coastal upwelling as the date at which (1) the thermocline had a shallow peak and (2) an upward thermocline displacement of more than 10 m was observed for the past 20 days. Finally, 12 upwelling events were identified, as shown in Figure 3 and Table 1. We also evaluated the definition using different criteria of thermocline (isotherm: 20° to 25°C isotherm or potential density: 24 to 25 σ_θ) and obtained similar results.

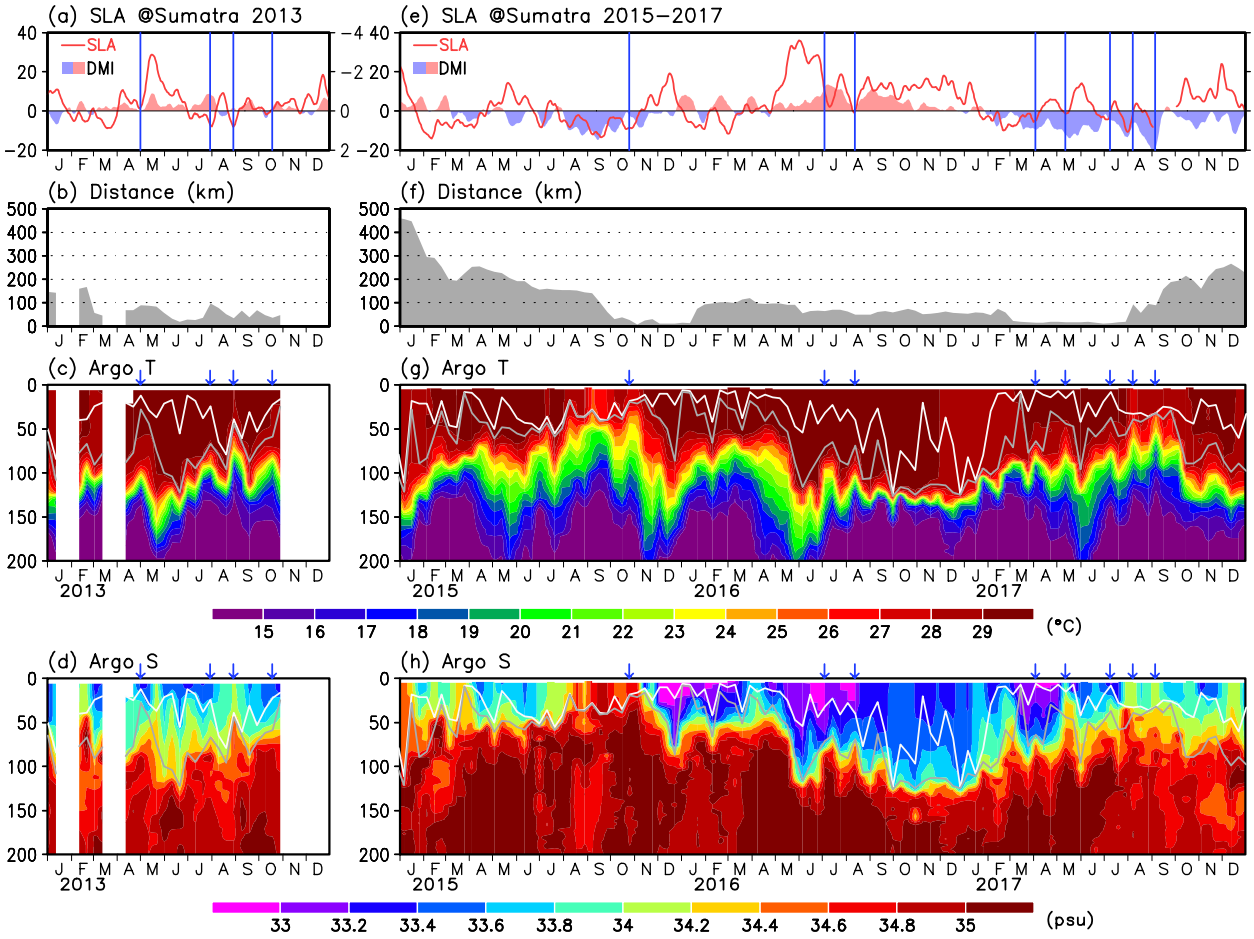

Figure 3. (a) Timeseries of sea level anomaly (SLA) (cm) during 2013 obtained from a tidal station on the southwest coast of Sumatra (black line) (left axis). (See Figure 2 for the location.) Red/blue shadings show Dipole Mode Index (DMI) (right axis). Note that the red shading indicates the negative DMI. (b) The distance (km) between the Argo float and the Sumatra coast. (c) Time-depth section of temperature observed by the Argo floats during 2013. The white and gray lines indicate the mixed layer depth (MLD) and the isothermal layer depth (ILD), respectively. (d) As in Figure 3c, but for salinity. (e–h) Same as in Figures 3a–3d, respectively, but for the data during 2015–2017. Coastal upwelling events observed by Argo floats are indicated by vertical lines in (a) and (e) and arrows in (c), (d), (g), and (h).

3.2. Observed features

During each upwelling season, the observed thermocline was relatively deep (shallow) in 2013 and 2016 (2015 and 2017) associated with the basin-scale anomalous SST condition of negative (positive) IOD that occurred in 2013 and 2016 (2015 and 2017) (Figures 3c and 3g). Except for 2016, seasonal upwelling signals were observed as the thermocline was gradually shoaling from June to August and had seasonal shallow peaks in August–September. Together with the seasonal variation, several intraseasonal variations of the thermocline were also observed during the upwelling season. Some of the intraseasonal variations were defined as coastal upwelling events (blue arrows in Figures 3c, 3d, 3g, and 3h). In more than half of the

upwelling events, the mixed layer, and hence the surface temperature variations were not obvious, which is different from the case for south of Java (Horii et al., 2018). In particular, in 2013 and 2016, the thermocline and isothermal layer were deep, with fewer cooling signals in the mixed layer during the upwelling season. The clear cases of SST cooling southwest of Sumatra were only observed in August–September of 2015 and 2017 during our study period (Figures 1b and 1c).

Table 1. List of observed coastal upwelling events observed by Argo floats along the southwest coast of Sumatra. The date shows the peak (day 0) of coastal upwelling events. The shoaling of the thermocline (25 °C isotherm) was calculated as the difference in the thermocline depth from day −20 to day 0. See Section 3.1 for how to estimate the distance to Sumatra.

Date	Thermocline shoaling	Distance to Sumatra (day 0)
1 May 2013	−23 m	89 km
30 Jul 2013	−30 m	97 km
29 Aug 2013	−41 m	35 km
18 Oct 2013	−14 m	36 km
25 Oct 2015	−24 m	26 km
4 Jul 2016	−21 m	64 km
12 Aug 2016	−28 m	50 km
3 Apr 2017	−11 m	14 km
12 May 2017	−25 m	17 km
9 Jul 2017	−13 m	14 km
7 Aug 2017	−46 m	93 km
5 Sep 2017	−36 m	88 km

The peaks of observed intraseasonal coastal upwelling events accompanied negative SLA peaks (Figures 3a and 3e). This indicates that the coastal upwelling system can be approximated by a two-layer model, as in Yoshida (1955). Exceptions were also observed for the events in October 2013, July 2016, and August 2017, probably due to the coarse time resolution (in other words, aliasing) of Argo observations. Argo observations every 10 days may not be enough to capture all of the intraseasonal signals, for example, 20–30-day periods. Using the same Indonesian sea level data for 2007-2012, Horii et al. (2016) found that the intraseasonal coastal upwelling signal was significant for the 20- to 50-day time scale. We checked the power spectrum of the SLA during the upwelling season in 2013–2017 and found the spectrum to be consistent with our previous results (figure not shown).

Seasonal and year-to-year salinity variations above the thermocline (6–120 dbar) were prominent together with intraseasonal-scale upward displacements of high-salinity signals (Figures 3d and 3h). As the large-scale ocean condition in the eastern Indian Ocean associated with IOD (Grunseich et al., 2011; Durand et al., 2013; Du and Zhang, 2015; Kido and Tozuka, 2017), the upper-layer salinity southwest of Sumatra tended to be fresh (saline) during negative (positive) IOD. Consistent with past CTD observations (Moteki et al., 2018), upper-ocean salinity stratification was common throughout the observation period likely due to continuous precipitation off Sumatra, forming an almost constant shallow mixed layer above the isothermal layer. Except for July–November 2015 and August–September 2017, the isothermal layer was

deeper than the mixed layer, and a thick barrier layer was observed. The shallow mixed layer and the thick barrier layer were related to upper-layer low-salinity signals, such as those observed in June–July 2013, June–September 2016, and April–July 2017. In general, intraseasonal-scale temperature and salinity variations were in phase at the thermocline depth. Note that subsurface high-salinity signals tended to reach the mixed layer, unlike the temperature variations. This suggests that the ocean vertical structure of the coastal upwelling system along Sumatra is characterized by salinity stratification in the deep isothermal layer.

To understand the general structure of the coastal upwelling events, we averaged timeseries based on the peaks of the upwelling (day 0) (Figure 4). On average, the thermocline (20 to 25°C) shoals more than 20 m from day −20 to day 0, and a high-salinity signal extends upward at the thermocline depth. On the 12×5 profiles used for the composite, the MLD is significantly 20 m shallower than the ILD at the 90% confidence limit, indicating robust existence of the barrier layer. The averaged shoaling signals of the MLD and the ILD from day −10 to day 0 were also statistically significant (90% level). There is less temperature variation at the mixed layer and, hence, at the sea surface. Although a decrease in surface salinity can be observed from day −10 to day 0, the average change was small (−0.1 psu) compared to the large variance among the events (0.34 psu). Therefore, the salinity signal was not statistically significant.

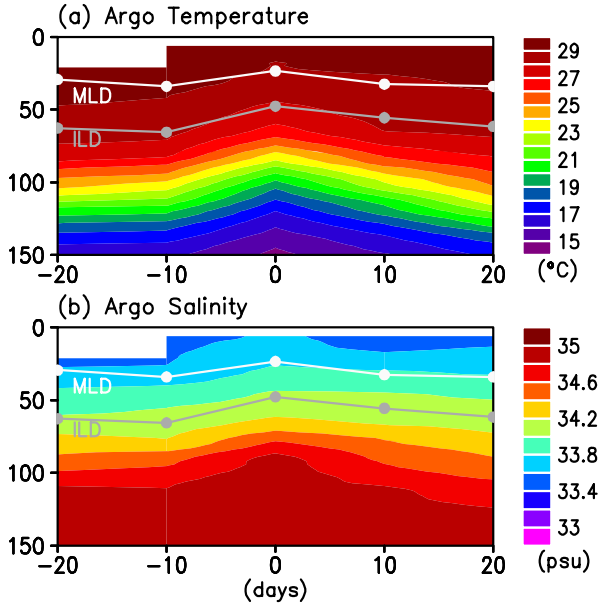

Figure 4. (a) Time-depth section of composite temperature based on 12 coastal upwelling events. The time axis is centered at each peak of an event. The white (gray) line indicates the MLD (ILD). (b) As in Figure 4a, but for salinity. Data are from the two Argo floats. (See Section 2.)

Each vertical structure of temperature and its time evolution during the coastal upwelling event is shown in Figure 5, together with intraseasonal-scale alongshore winds and sea level variations at Sumatra. In general, alongshore southeasterly winds led the coastal upwelling signals. For example, winds led sea level depression and thermocline shoaling by approximately 5 to 15 days (Figures 5a, 5c, 5f, and 5g). The averaged winds include equatorial zonal winds, because the coastal region can be influenced by equatorial zonal wind forcing and subsequent

Kelvin wave propagation (Iskandar et al., 2005; Drushka et al., 2010; Delman et al., 2016; 2018). Exceptions are also observed in several cases, as in Figures 5d, 5e, 5h, 5i, and 5j. The barrier layer thickness (BLT) varied in the events, such as a thick barrier layer of more than 50 m before the peak (Figures 5a, 5b, 5f, and 5g) and a thin barrier layer of less than 10 m at the peak (Figures 5c, 5e, 5k, and 5i). The BLT tended to decrease around each peak because of the shoaling of the ILD. Note that in events when cold water reached the surface mixed layer, the ILD and MLD became understandably equal so that no thick barrier layer was observed (Figures 5c, 5e, 5k, and 5l).

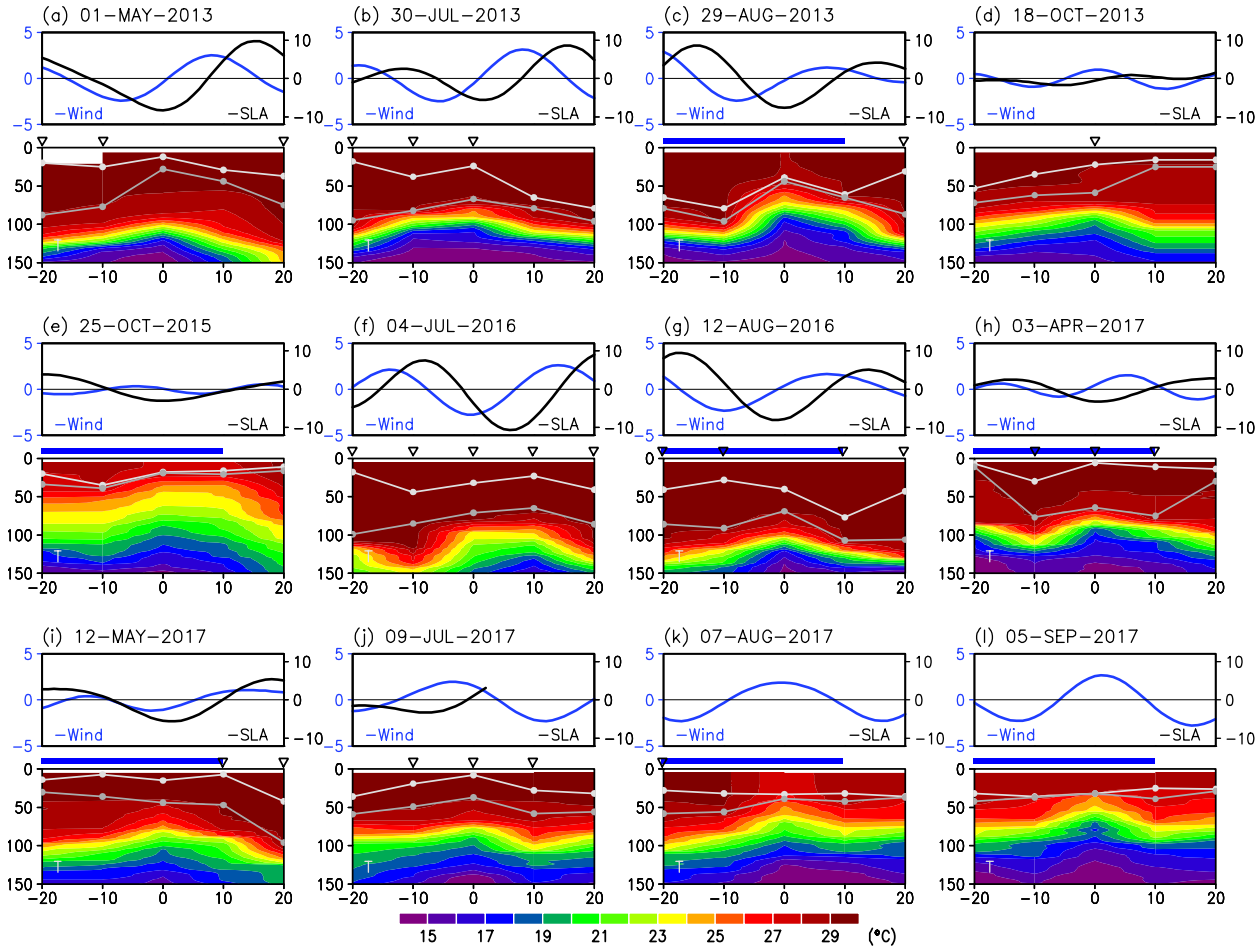

Figure 5. Area-averaged winds along the equator and the Sumatra coast (80°E–105°E; blue line in each upper panel with the scale of the left axis: m s−1), SLA as in Figure 3a (black line with the right axis: cm), and time-depth section of temperature observed by Argo floats (each bottom panel) for the 12 coastal upwelling events. The period is from day −20 to day +20 and centered at the peak of the upwelling event (day 0). The white (gray) line shows MLD (ILD). The horizontal blue line shows the period for which mixed layer temperature (MLT) cooling < −0.2 °C was observed (See Figure 8). The triangle shows the barrier layer thicker than 30 m. The winds and the SLA data were filtered using a 101-point Lanczos filter to extract 20- to 50-day signals.

Precipitation signals were observed with the coastal upwelling observations (Figure 6). Except for the case in October 2015, there were precipitation signals of varying degree. Relatively rich (poor) rainfall during 2013 and 2016 (2015 and 2017) would have been due to large-scale enhanced (reduced) atmospheric convection around the Maritime Continent associated with the negative (positive) IOD during the upwelling season (Grunseich et al., 2011; Durand et al., 2013; Horii et al., 2013; Du and Zhang, 2015). The precipitation accompanied surface low-salinity signals, upper-layer stratification, and thick barrier layer. In some cases, the surface low-salinity signals were canceled with upwelling signals of high-salinity water (Figures 6c, 6i, 6k, and 6l). In such cases, the barrier layer tended to be thin during the upwelling events. A systematic change in precipitation was not observed before and after the peak of the upwelling event.

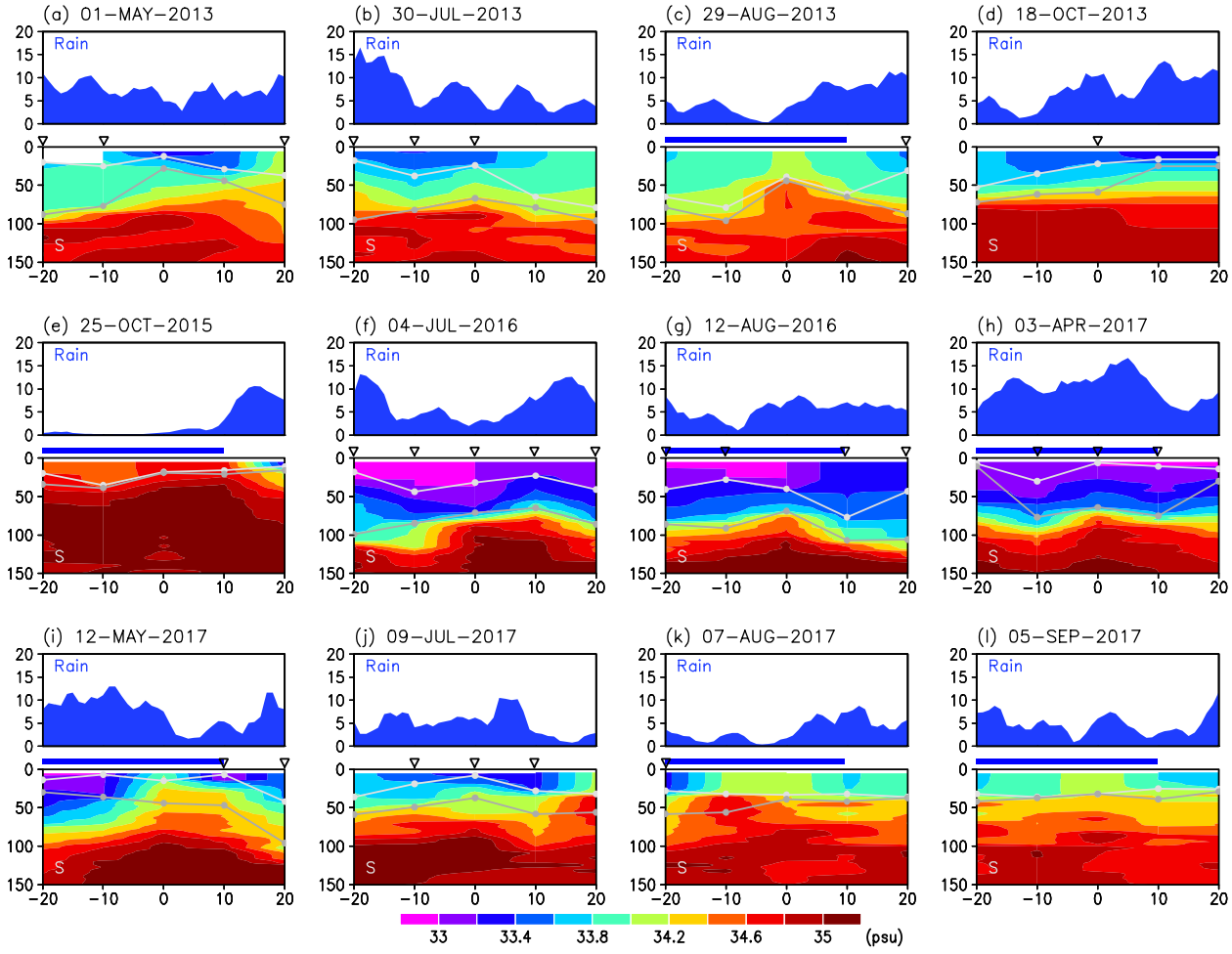

Figure 6. As in Figure 5, but for precipitation (blue timeseries in each upper panel: mm day−1) around the average Argo observation points of coastal upwelling peaks (5°×5° box: 100.5°E–105.5°E, 7.5°S–2.5°S) and time-depth section of salinity (each bottom panel). The precipitation data were smoothed with a 5-day running mean filter.

Correlation analysis between the Argo salinity observation and the satellite-based precipitation suggests that the observed surface salinity signals were associated with local precipitation around the observation points (Figure 7). Significant correlation spreads around the Argo observation points, including south of Sumatra and north of Java, with a peak around 99°E–103°E, 9°S–6°S. The surface low salinity signals (Figure 6) would be related to a series of regional precipitation system southwest of Sumatra and their subsequent advection. River runoff from southern Sumatra would also contribute to the salinity signals. The reason for the peak of the correlation being several hundred kilometers southwest from surface salinity observations remains unknown, and the rigorous freshwater and salinity budget in the coastal region will be the subject of a future study.

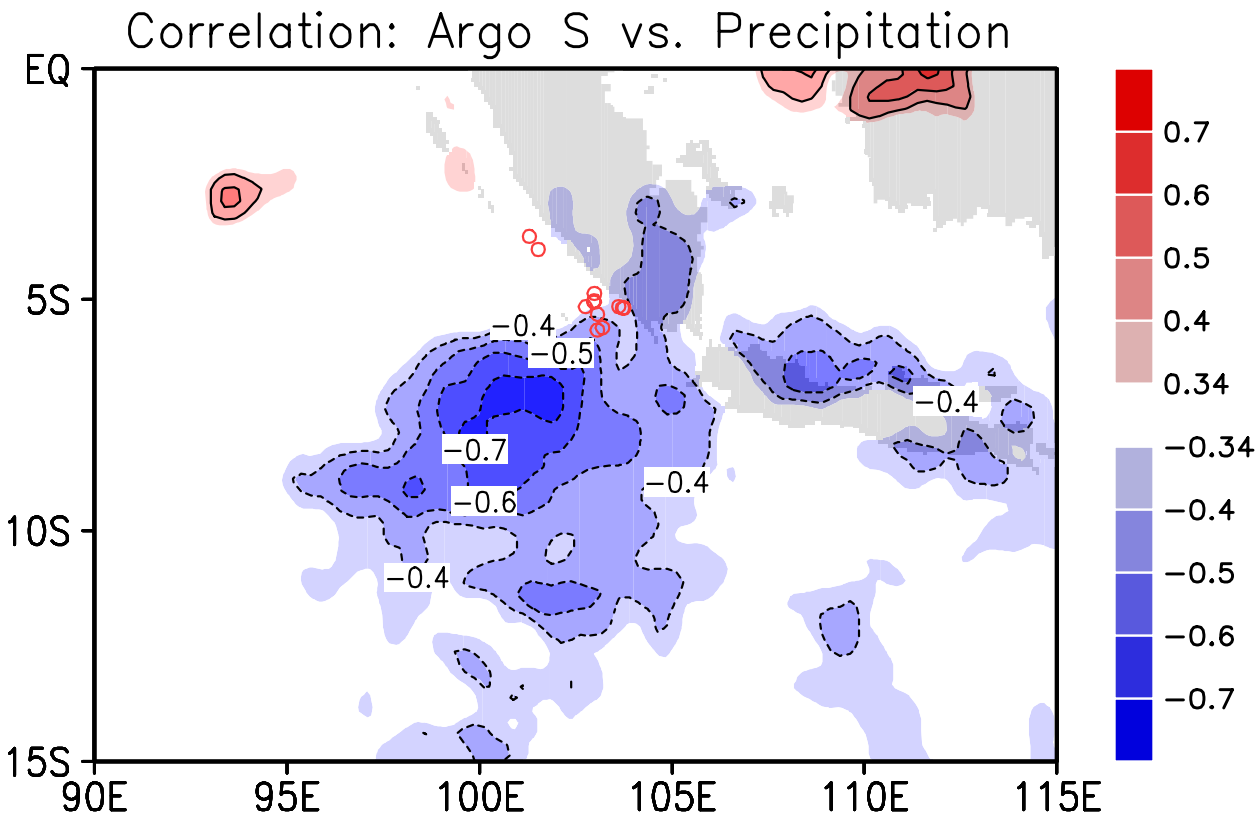

Figure 7. Correlation coefficients of satellite-based precipitation with upper-layer (6–25 db) salinity observed by Argo. The Argo salinity data for day −10 and day 0 during 12 upwelling events were used (sampling number: 24). Red circles indicate locations of observed coastal upwelling events. The precipitation data were smoothed with a 5-day running mean filter before computation. The coefficients exceeding 0.34, 0.40, and 0.51 are statistically significant at the 90%, 95%, and 99% levels, respectively.

3.3. Salinity stratification and temperature change

To investigate the characteristics of coastal upwelling events associated with the background condition, we observed the relationships among the MLT, the thermocline depth,

and the salinity variations of the events (Figure 8). Temporal changes in the MLT during the events are significantly correlated with the background mean MLT and the thermocline depth (Figures 8a and 8b), respectively. This suggests that cold water upwelling tends to reach the mixed layer when the thermocline is shallow. Note that MLT variations are not simply controlled by the vertical process. Surface heat exchanges also contribute to the MLT variation and would naturally increase the variation in the scatterplots.

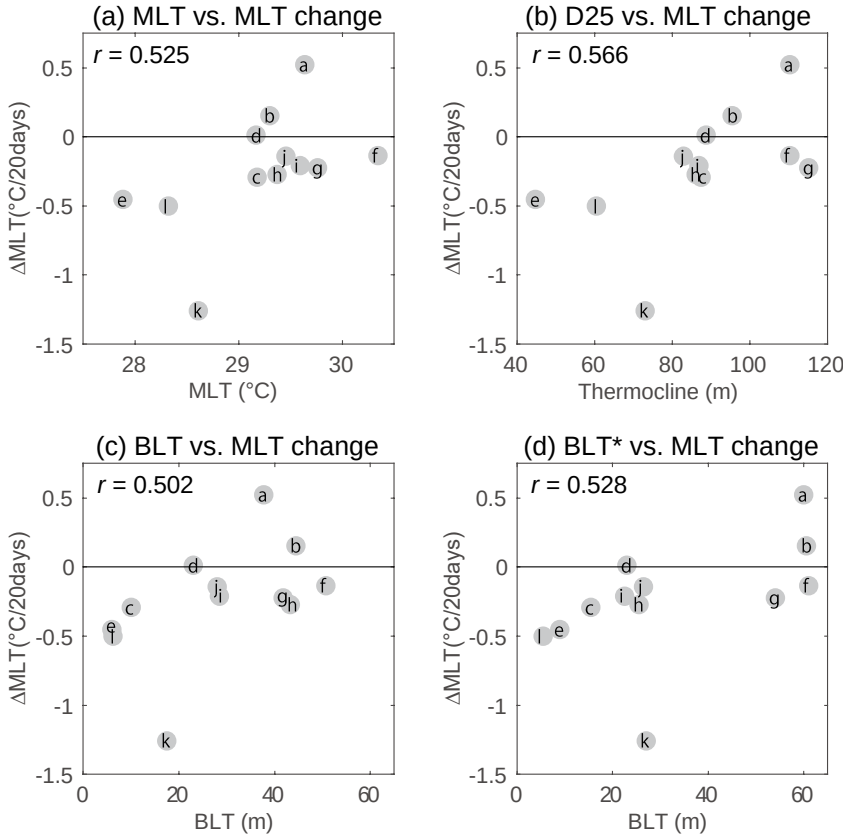

Figure 8. Scatter plots of properties observed during the 12 upwelling events: (a) the mixed layer temperature (MLT) vs. the temporal change in the MLT (ΔMLT); (b) thermocline depth vs. ΔMLT; (c) the barrier layer thickness (BLT) vs. ΔMLT. The MLT, the thermocline depth, and the BLT are averaged during upwelling events from day −20 to day +10. (d) As in Figure 8c, but averaged from day −20 to day −10. Here, ΔMLT was defined as the difference in MLT from day 0 to day +10 and that from day −20 to day −10. The alphabets (a–l) denote the coastal upwelling events shown in Figures 5a–5l and 6a–6l (e.g., 'a' is the event on 1-May-2013). The correlation coefficients are shown in the panels. Correlation greater than 0.48 is statistically significant at the 90% level.

As shown in Figure 6, upwelling signals likely associate upper-layer salinity stratification and barrier layer. The MLT changes are also significantly correlated with the background BLT averaged from day −20 to day +10 (Figure 8c). The largest MLT cooling (ΔMLT: −1.3°C) was observed on 7 August 2017 (See also Figure 5k). We note that the correlation of the MLT

changes and the BLT was still significant (0.54) after removing this strongest case. Interestingly, the MLT changes are also correlated with the BLT averaged 'before' the upwelling peaks (from day −20 to day −10), with a significant correlation of 0.53 (Figure 8d). This implies that the background stratification has some effect on the MLT variations through changing the vertical process during the coastal upwelling events. This may be a possible consequence, given that the cooling at the bottom of the mixed layer is suppressed under the condition of a shallow mixed layer and a deep isothermal layer (and thus also the thick barrier layer). Details of the possible processes will be further discussed in Section 5.

To further investigate the background condition related to the BLT, we checked the upper-layer (6–25 db) salinity, the MLD, and the ILD among the events (Figure 9). The BLT correlates well with upper-layer salinity and the ILD, respectively (Figures 9a and 9b), suggesting that upper-layer stratification and/or a deep isothermal layer are essential for the thick barrier layer. On the other hand, there was no significant correlation between the MLD and the BLT (Figure 9c). This is most likely because the MLD is influenced by various processes, such as surface heat and momentum forcing, and cannot be explained by the surface freshwater flux alone.

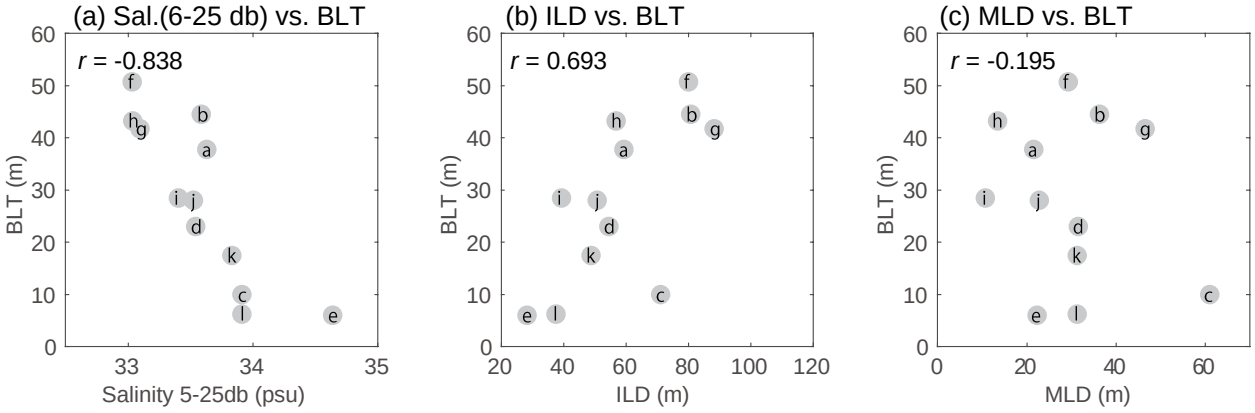

Figure 9. As in Figure 8, but for (a) salinity averaged for 5–25 db vs. the BLT; (b) isothermal layer depth (ILD) vs. the BLT; and (c) the MLD and the BLT. The BLT was defined as in Figure 8. The salinity, the ILD, and the MLD are averaged from day −20 to day +10.

4 Large-scale atmospheric variation and coastal upwelling

In this section, we analyze regional to large-scale atmospheric conditions that generated anomalous winds and precipitation in the eastern tropical Indian Ocean associated with coastal upwelling southwest of Sumatra. Since the sea level variation at Padang (0.95°S, 100.37°E; Figure 2) is closely related to the upwelling signals (Figures 3 and 5), we re-defined intraseasonal coastal upwelling events using the sea level data. We focused on the period of 2007–2012, during which we obtained the sea level timeseries with fewer missing values. We applied a 20- to 50-day band-pass filter to extract intraseasonal signals. Using a threshold of 1.0 standard deviation, we selected 33 cases with significant negative sea level peaks. We obtained almost the same signals using the Real-Time Multivariate MJO Index (Wheeler and Hendon

2004). The increased sample numbers would elucidate the general atmospheric condition associated with the upwelling. We checked the results with minor modification of the threshold and the cutoff period and confirmed that no fundamental difference in the results was produced.

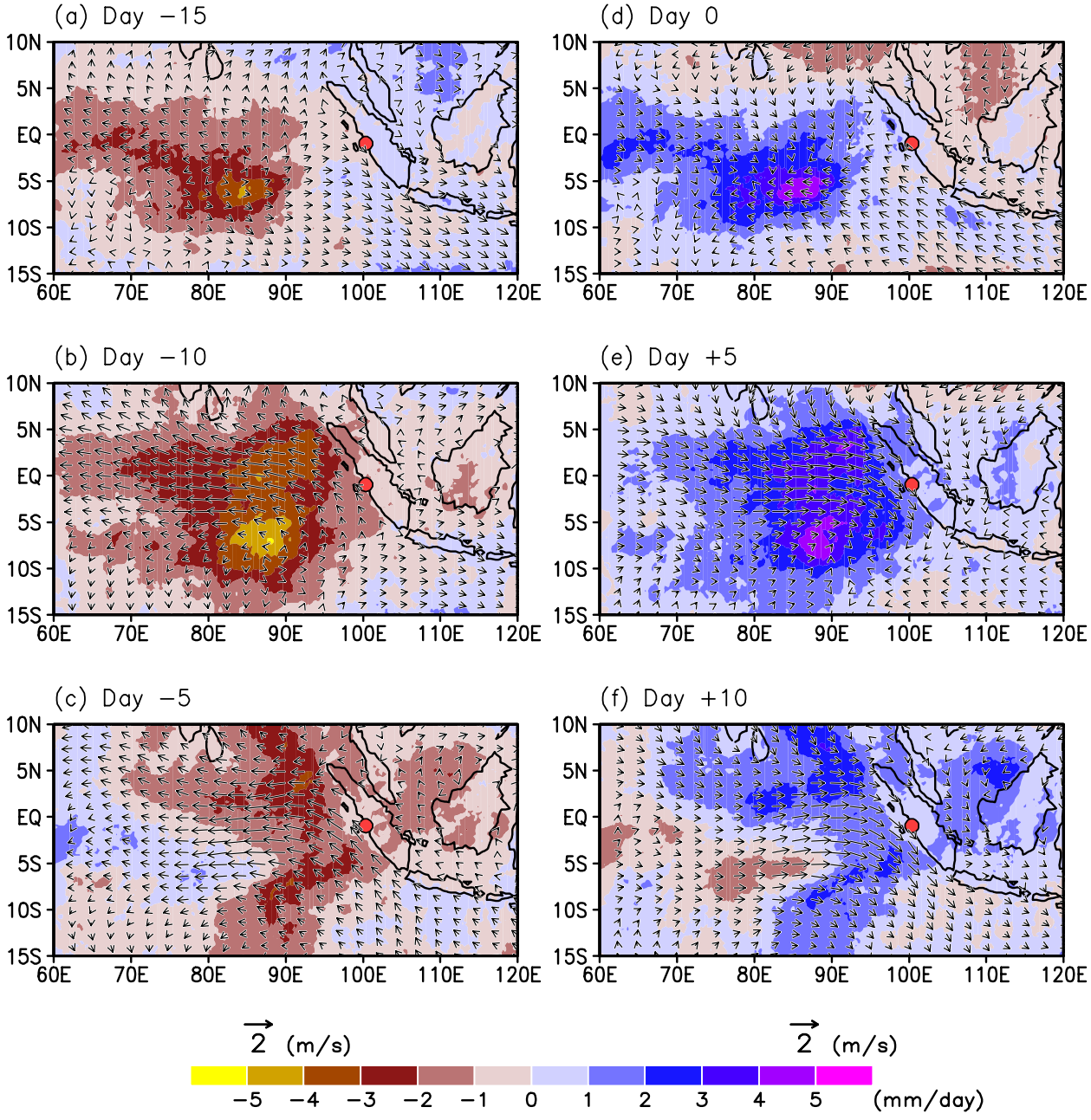

Figure 10. Composite maps of intraseasonal-scale (20- to 50-day filtered) precipitation anomalies (color shading) and surface wind anomalies (vector) based on 33 upwelling peaks (day 0) described in Section 4. The peaks were defined using the sea level variations at Padang (red circle). The time shown with each plot is relative to the peak of the upwelling events.

Consistent with past studies (Chen et al., 2015; Horii et al., 2016; 2018; Cao et al., 2019), intraseasonal coastal upwelling was found to have occurred with anomalous equatorial easterly winds and southeasterly winds off Sumatra (Figure 10). The anomalous southeasterly winds were identified as a part of eastward-propagating atmospheric system. On day −15, anomalous easterly winds first appeared in the central equatorial Indian Ocean (60°E–80°E), were enhanced and extended to the east on day −10, and then propagated eastward as southeasterly wind anomalies appeared along the coasts of Sumatra and Java from day −10 to day 0. After day 0 (upwelling peaks), wind anomalies turned westerly and northwesterly, respectively, over the equatorial Indian Ocean and along the coasts of Sumatra, and the upwelling events ended.

The propagation of the atmospheric system was accompanied by precipitation anomalies, namely an anomalous dry phase before the upwelling peaks (from day −15 to day −5) and a subsequent wet phase (from day 0 to day +10) in the eastern tropical Indian Ocean. This intraseasonal-scale atmospheric pattern is consistent with the propagation of MJO or boreal-summer intraseasonal oscillation (Lau and Chan, 1986; Lawrence and Webster, 2002). These signals were partly identified at in-situ observations, as leading an anomalous southeasterly wind and relatively dry (wet) conditions around day −10 to day 0 (day 0 to day +10) (e.g., Figures 5c, 5f, 6c, 6e, and 6f). Note that these precipitation anomalies visit 'after' the upwelling peaks and do not explain the precipitation signals often observed before the coastal upwelling events (Figure 6). However, precipitation was found to have occurred before the upwelling peaks (Figures 6 and 7). These results suggest that surface freshwater signals and upper ocean stratification cannot be simply explained by a systematic response to MJO/ISO. The precipitation may be from diurnal precipitation off Sumatra, which was not associated with atmospheric intraseasonal variation (Mori et al., 2004; Fujita et al., 2013).

Thermocline variation off Sumatra is strongly affected by equatorial zonal wind forcing in the central-eastern Indian Ocean through propagation of oceanic Kelvin waves (Iskandar et al., 2005; 2006; Drushka et al., 2010). The remote impact from basin-scale atmospheric forcing partly explains the thick barrier layer observed with coastal upwelling events. Figure 11 shows intraseasonal atmospheric forcing and ocean response along the equator and the coasts of Sumatra and Java. As shown in Figure 10, propagating atmospheric anomalies are observed as the dry and easterly condition (the wet and westerly condition) around day −15 to day 0 (day 0 to day +10) in the central to eastern Indian Ocean (Figures 11a and 11b). In the oceanic signal, the negative SLA appears as eastward propagating upwelling Kelvin waves along the equator (day −10 to day 0) and along the coasts of Sumatra and Java (day 0 to day +5), consistent with the phase speed of the first baroclinic mode (Figure 11c). Note that the propagations of oceanic signals (2.0–2.5 m s^{-1}) are relatively slow compared to those of atmospheric anomalies (5–6 m s^{-1}: typical propagation speed of MJO/ISO). Before the dry and easterly condition, there are equatorial westerly wind anomalies and subsequent downwelling Kelvin waves propagate and would cause deep thermocline anomalies around day −20 to day −5 off Sumatra. The deep thermocline anomalies are favorable to a thick isothermal layer. The deep isothermal layer and resultant thick barrier layer frequently observed at day −20 to day −10 (Figure 5) would thus partly be explained by the remote forcing. When a downwelling Kelvin wave arrives off Sumatra, intraseasonal-scale local atmospheric forcing has already turned southeasterly phase and started driving coastal upwelling. In this case, the signal southwest of Sumatra tends to be suppressed due to the cancellation between the local southeasterly wind and the remotely-forced downwelling Kelvin wave.

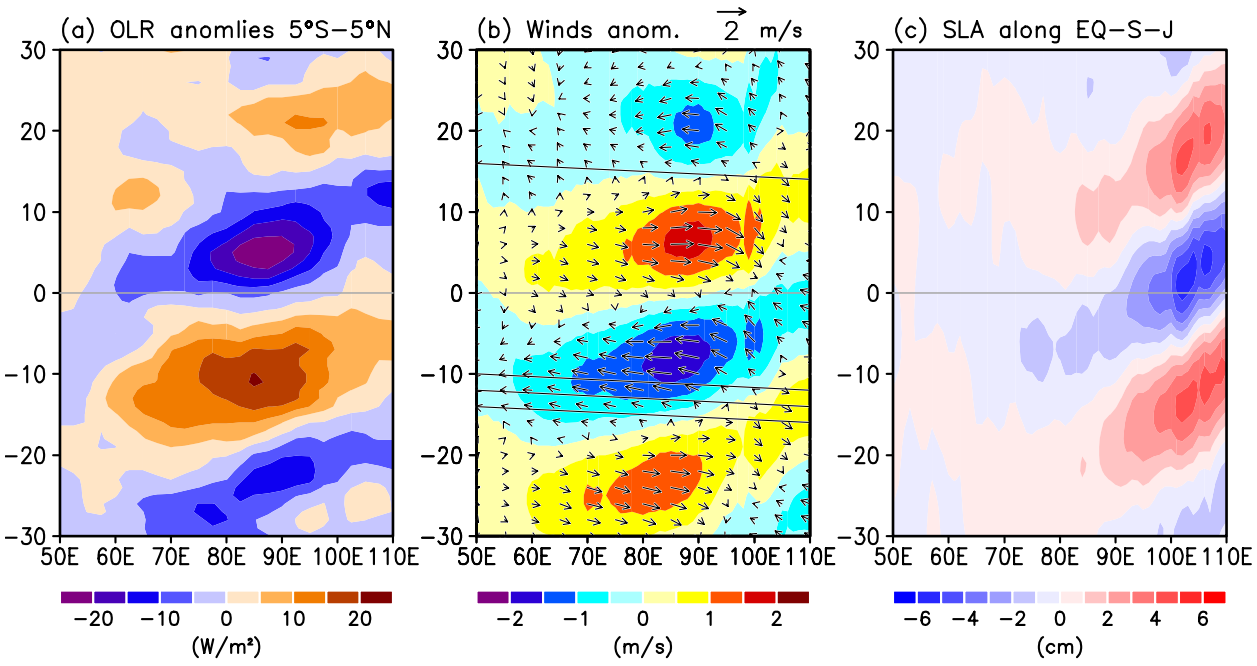

Figure 11. Longitude-time diagrams of band-pass filtered (a) outgoing longwave radiation (OLR), (b) winds, and (c) SLA. Composite anomalies based on 33 upwelling events described in Section 4. The OLR is averaged for 5°S–5°N. The winds and SLA are along the equator (50°E–98°E) and along the coasts of Sumatra and Java (98°E–110°E). The color shading in Figure 11b indicates the winds along the equator and along the coasts.

Finally, we investigated the characteristics of coastal upwelling events in terms of the large-scale background condition, i.e., Indian Ocean Dipole. A positive (negative) IOD causes anomalously cool (warm) SST and a shallow (deep) thermocline in the eastern Indian Ocean, including off Sumatra (Saji et al., 1999). As expected, the MLT and the thermocline depth correlates well with the DMI (Figures 12a and 12b). The temporal change in the MLT also significantly correlates with the DMI (Figure 12c). These results strongly suggest that the background shallow (deep) thermocline was a favorable (not favorable) condition for the MLT cooling during the coastal upwelling events.

The BLT is also correlated with the DMI (Figure 12d), which most likely reflects decreased (increased) precipitation and reduced (enhanced) upper ocean stratification in the eastern Indian Ocean during positive (negative) IOD. Upwelling events during negative IOD (DMI < −0.4) was always accompanied by a thick barrier layer, although the sampling number is quite small (3). Anomalous equatorial westerly winds during the negative IOD is favorable for a deep isothermal layer. These results suggest that the IOD is a major factor in setting the ocean vertical structure associated with the coastal upwelling southwest of Sumatra. Note that during the positive IOD (defined here as DMI > 0.4) the MLT, the thermocline depth, ΔMLT, and the BLT were quite different among upwelling events. The ocean vertical structure off Sumatra was highly variable, even if a moderate positive IOD was occurring in the background. For example, temperature and salinity variations during the upwelling events on July 2017 and August 2017 were quite different in terms of MLT changes and upward displacements of high salinity signals (Figures 5j, 5k, 6j, and 6k). Both the large-scale atmosphere and ocean condition and

local/regional forcing must play roles in controlling temperature and salinity variations during the upwelling events.

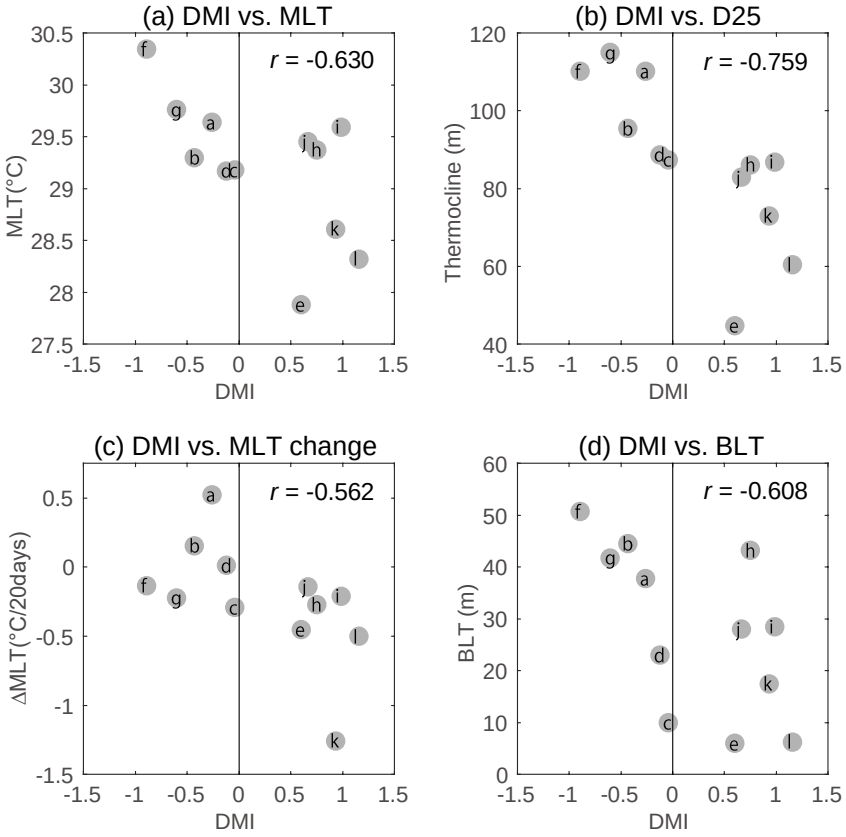

Figure 12. Figure 12. Scatter plots of DMI and properties observed during the 12 upwelling events: (a) MLT, (b) ΔMLT, and (c) BLT. The DMI are averaged for the period of upwelling events from day −20 to day +10. The MLT, ΔMLT, and BLT are as in Figure 8.

5 Discussion and conclusions

We have presented the ocean vertical structure of temperature and salinity variations in the coastal upwelling region along the coast of Sumatra based on timeseries of two Argo floats. The observation data captured intraseasonal-scale upwelling events, as shown by upward displacements of thermocline and high-salinity water, with leading anomalous local southwesterly winds and equatorial easterly winds. These results constitute the first observation-based overview of the coastal upwelling system focusing on the intraseasonal variations while also showing the seasonal and year-to-year variations.

The observed MLT (and hence the SST) variations during the intraseasonal upwelling events were found to be rather small, despite the significant thermocline variations. These small surface signals may have been thought to be due to the background deep thermocline. Observational data suggested this to be the case. No/less surface signal was observed when the background thermocline was deep, as seen during the upwelling season in 2016. In the present

study, we also have observed salinity stratification and a frequently-formed thick barrier layer in the upwelling region. In the intraseasonal upwelling events, a statistical relationship was observed between the MLT variations and the background barrier layer. This result can be partly understood as a response to the large-scale atmosphere and the ocean condition in the tropical Indian Ocean. During the positive (negative) IOD, precipitation tends to decrease (increase) and the thermocline tends to be shallow (deep) in the eastern Indian Ocean, including around Sumatra (Grunseich et al., 2011; Durand et al., 2013; Du and Zhang, 2015), forming a reduced (enhanced) upper-ocean salinity stratification and a thin (thick) barrier layer. Concurrently, the shallow (deep) thermocline provides a favorable (unfavorable) condition for the appearance of the subsurface upwelling signal to the surface. In addition, the intraseasonal coastal upwelling events were different in terms of MLT variation and ocean vertical structure (Figures 5 and 6), even if these events occurred in a similar large-scale background condition. For example, the MLT, upper ocean stratification, and the BLT were different in same upwelling season as in the three events that occurred during the period of July–October 2013 (neutral IOD condition; Figures 5b–5d and 6b–6d) and in two events during July–September 2017 (positive IOD condition; Figures 5k–5l and 6k–6l). Thus, the results may provide some evidence that the upper ocean salinity controls the local SST through changing vertical stratification in the coastal upwelling system.

The process can be explained as follows if the background salinity controls the local SST through changing ocean vertical structures in the coastal upwelling system. For example, suppose the case of a commonly observed vertical profile with a shallower mixed layer and a salinity stratification below, over a deeper isothermal layer. In the coastal upwelling system, surface alongshore winds cause surface mass divergence with offshore Ekman transport. The resultant coastal upwelling generates upward displacement of the ocean vertical structure. There, ocean surface momentum forcing and radiative forcing tend to be trapped in the shallow mixed layer because of the presence of the barrier layer (Lukas and Lindstrom, 1991; Sprintall and Tomczak, 1992). Thus, the salinity stratification and deep isothermal layer would provide an unfavorable condition for the entrainment of subsurface cold water to the mixed layer above. Although the term ‘barrier layer’ was originally used in the context of the ‘barrier’ of surface forcing, the foregoing explanation may clarify the role of the barrier layer in preventing the signal from the subsurface. This point requires further support from observations and/or numerical studies.

Assuming that the above hypothesis holds, frequent and sporadic freshwater input off Sumatra could limit the cold-water upwelling and subsequent advection to the eastern pole of the IOD during the positive IOD. Future changes in precipitation and stratification off Sumatra will also affect the IOD development. For example, possible future decrease of boreal summer precipitation in the eastern Indian Ocean and Maritime Continent (Kang et al., 2019) will reduce stratification and will have a positive effect on the development of the positive IOD. Some studies have also shown that the extreme positive IOD will be more frequent in the future (e.g., Cai et al., 2014). In such extreme cases, the precipitation in the eastern Indian Ocean is sufficiently suppressed, causing reduced stratification, efficient entrainment cooling and anomalously cold SST development under the Bjerknes feedback.

It is worth noting that the sampling number was rather small (12 cases) in the present study. Further study is necessary in order to clarify the possible relationship between upper ocean stratification and MLT (SST) variations in the coastal upwelling system. The process

583 suggested in the present study is one dimensional and does not consider horizontal advection and
584 surface heating/cooling. Mesoscale and sub-mesoscale circulation, recently reported for other
585 coastal upwelling systems, should also be considered in a future study. The timeseries presented
586 here will be useful for validating high-resolution numerical models. Using these models, heat
587 and freshwater budget analyses are desirable in a future study. Recent satellite observation of
588 surface salinity will also help to estimate horizontal gradient and advection of freshwater in the
589 intraseasonal time scale.

590 The present study provides observation of coastal upwelling, which is considered to be an
591 important component for IOD development. As inferred from SST distribution (Figure 1),
592 variations in the coastal region would include much smaller horizontal-scale variations, as
593 compared to large-scale climate variations like the IOD. The presented results still tell us little
594 about the horizontal difference. Understanding the interaction between such small-scale coastal
595 upwellings and the large-scale IOD remains a challenge, and future studies to quantify the
596 possible contribution of coastal upwelling to horizontal heat transport are needed.

597

598 **Acknowledgments**

599 AQC Argo data version 1.2 produced by JAMSTEC is used for this study (available online at
600 http://www.jamstec.go.jp/ARGO/argo_web/argo/?page_id=100&lang=en). We thank the
601 following data providers: quality-controlled sea level data from tide gauges were provided by
602 UHSLC (http://uhslc.soest.hawaii.edu); sea level pressure data and OISST data were provided by
603 NOAA/OAR/ESRL PSD (https://www.esrl.noaa.gov/psd/); wind data of the ASCAT satellite
604 were provided by the Centre de Recherche et d'Exploitation Satellitaire (CERSAT) at
605 IFREMER, obtained through Asia-Pacific Data-Research Center (APDRC;
606 http://apdrc.soest.hawaii.edu/); PERSIANN rainfall data was provided by the CHRS
607 (https://chrsdata.eng.uci.edu/); gridded SLA data was provided by Copernicus–Marine
608 Environment Monitoring Service (http://marine.copernicus.eu/). MJO index was provided by
609 Bureau of Meteorology, Australia (http://www.bom.gov.au/climate/mjo/). We thank K. Richards
610 for helpful discussions. This study was supported by the Japan Society of the Promotion of
611 Science (JSPS) Grants-in-Aid for Scientific Research, 18K03753.

612

613 **References**

614 Aldrian, E., & Susanto, R. (2003). Identification of three dominant rainfall regions within
615 Indonesia and their relationship to sea surface temperature. *International Journal of*
616 *Climatology*, 23(12), 1435–1452, doi:10.1002/joc.950

617 Akima, H. (1970). A new method of interpolation and smooth curve fitting based on local
618 procedures, *Journal of the Association for Computing Machinery*, 17, 589–602.

619 As-syakur, A. R., Osawa, T., Miura, F., Nuarsa, I. W., Ekayanti, N. W., Dharma, I. G. B. S.,
620 Adnyana, I. W. S., Arthana, I. W., & Tanaka, T. (2016). Maritime continent rainfall
621 variability during the TRMM era: the role of monsoon, topography and El Niño Modoki.
622 *Dynamics of Atmospheres and Oceans*, 75, 58−77.

Bentamy, A., & Fillon, C. D. (2012). Gridded surface wind fields from Metop/ASCAT measurements. *International Journal of Remote Sensing*, 33(6), 1729-1754.

Bray, N. A., Hautala, S., Chong, J. C., & Pariwono J. (1996). Large-scale sea level, thermocline, and wind variations in the Indonesian Throughflow region. *Journal of Geophysical Research: Oceans*, 101, 12239–12254.

Cai, W., Santoso, A., Wang, G., Weller, E., Wu, L., Ashok, K., Masumoto, Y., & Yamagata, T. (2014). Increased frequency of extreme Indian Ocean Dipole events due to greenhouse warming. *Nature*, 510(7504), 254–258. https://doi.org/10.1038/nature13327

Cao, G., Xu, T., He, Y., Wang, L., Wang, D., Wei, Z., & Zhu, Y. (2019). Seasonality in intraseasonal sea surface temperature variability along the Sumatra-Java southern coast. *Journal of Geophysical Research: Oceans*, 124. https://doi.org/10.1029/2018JC014853

Caldwell, P. C., Merrifield, M. A., & Thompson, P. R. (2015). Sea level measured by tide gauges from global oceans as part of the Joint Archive for Sea Level (JASL) from 1846-01-01 to 2015-07-31. National Oceanographic Data Center, NOAA. https://doi.org/10.7289/V5V40S7W

Charney, J. G. (1955). The generation of oceanic currents by winds, *Journal of Marine Research*, 14, 477-498.

Chen, G., Han, W., Li, Y., Wang, D., & Shinoda, T. (2015). Intraseasonal variability of upwelling in the equatorial Eastern Indian Ocean. *Journal of Geophysical Research: Oceans*, 120, 7598–7615. https://doi.org/10.1002/2015JC011223

Chen, G., Han, W., Li, Y., & Wang, D. (2016). Interannual variability of equatorial eastern Indian Ocean upwelling: Local vs. remote forcing. *Journal of Physical Oceanography*, 46, 789–807.

Delman, A. S., Sprintall, J., McClean, J. L., & Talley, L. D. (2016). Anomalous Java cooling at the initiation of positive Indian Ocean Dipole events. *Journal of Geophysical Research: Oceans*, 121, 5805–5824. https://doi.org/10.1002/2016JC011635

Delman, A. S., McClean, J. L., Sprintall, J., Talley, L. D., & Bryan, F. O. (2018). Process-specific contributions to anomalous Java mixed layer cooling during positive IOD events. *Journal of Geophysical Research: Oceans*, 123. https://doi.org/10.1029/2017JC01374

Drushka, K., Sprintall, J., Gille, S. T., & Brodjonegoro, I. (2010). Vertical structure of Kelvin waves in the Indonesian throughflow exit passages. *Journal of Physical Oceanography*, 40(9), 1965– 1987. https://doi.org/10.1175/2010jpo4380.1

Du, Y., & Zhang, Y. (2015). Satellite and Argo observed surface salinity variations in the tropical Indian Ocean and their association with the Indian Ocean Dipole mode. *Journal of Climate*, 28(2), 695–713. https://doi.org/10.1175/JCLI-D-14-00435.1

Du, Y., Meyers, G., Masumoto, Y., & Sasaki, H. (2005). Seasonal heat budget in the mixed layer of the southeastern tropical Indian Ocean in a high-resolution ocean general circulation model. *Journal of Geophysical Research: Oceans*, 110, C04012. https://doi.org/10.1029/2004JC002845

Du, Y., Qu, T., & Meyers, G. (2008). Interannual variability of sea surface temperature off Java and Sumatra in a global GCM. *Journal of Climate*, 21(11), 2451– 2465. https://doi.org/10.1175/2007JCLI1753.1

Durand, F., Alory, G., Dussin, R., & Reul, N. (2013). SMOS reveals the signature of Indian Ocean Dipole events. *Ocean Dynamics*, 63(11-12), 1203-1212. https://doi.org/10.1007/s10236-013-0660-y

Fujita, M., Takahashi, H. G., Hara, M. (2013). Diurnal cycle of precipitation over the eastern Indian Ocean off Sumatra Island during different phases of Indian Ocean Dipole. *Atmospheric Science Letters*, 14(3), 153-159, doi:10.1002/asl2.432

Grumet, N. S., Abram, N. J., Beck, J. W., Dunbar, G. B., Gagan, M. K., Guilderson, T. P., Hantoro, W. S., & Suwargadi, B. W. (2004). Coral radiocarbon records of Indian Ocean water mass mixing and wind-induced upwelling along the coast of Sumatra, Indonesia. *Journal of Geophysical Research: Oceans*, 109, C05003. https://doi.org/10.1029/2003JC002087

Grunseich, G., Subrahmanyam, B., Murty, V. S. N., & Giese, B. S. (2011). Sea surface salinity variability during the Indian Ocean Dipole and ENSO events in the tropical Indian Ocean. *Journal of Geophysical Research: Oceans*, 116(C11), C11013. https://doi.org/10.1029/2011JC007456

Halkides, D. J., & Lee, T. (2009). Mechanisms controlling seasonal-to-interannual mixed layer temperature variability in the southeastern tropical Indian Ocean. *Journal of Geophysical Research: Oceans*, 114, C02012, doi:10.1029/2008JC004949

Hanawa, K., & Mitsudera, H. (1985). On the data processing of daily mean values of oceanographic data: Note on the daily mean sea-level data (in Japanese). *Bulletin on Coastal Oceanography*, 23, 79–87.

Horii, T., Masumoto, Y., Ueki, I., Hase, H., & Mizuno, K. (2009). Mixed layer temperature balance in the eastern Indian Ocean during the 2006 Indian Ocean dipole. *Journal of Geophysical Research: Oceans*, 114, C07011. https://doi.org/10.1029/2008JC005180

Horii, T., Ueki, I., Ando, K., & Mizuno K. (2013). Eastern Indian Ocean warming associated with the negative Indian Ocean dipole: A case study of the 2010 event. *Journal of Geophysical Research: Oceans*, 118, 536–549, doi:10.1002/jgrc.20071

Horii, T., Ueki, I., Syamsudin, F., Sofian, I., & Ando, K. (2016). Intraseasonal coastal upwelling signal along the southern coast of Java observed using Indonesian tidal station data. *Journal of Geophysical Research: Oceans*, 121, 2690– 2708. https://doi.org/10.1002/2015JC010886

Horii, T., Ueki, I., & Ando, K. (2018). Coastal upwelling events along the southern coast of Java during the 2008 positive Indian Ocean Dipole. *Journal of Oceanography*. 74 (5), 499–508, doi: 10.1007/s10872-018-0475-z

Iskandar, I., Mardiansyah, W., Masumoto, Y., & Yamagata, T. (2005). Intraseasonal Kelvin waves along the southern coast of Sumatra and Java. *Journal of Geophysical Research: Oceans*, 110, C04013. https://doi.org/10.1029/2004JC002508

Iskandar, I., Tozuka, T., Sasaki, H., Masumoto, Y., & Yamagata, T. (2006). Intraseasonal variations of surface and subsurface currents off Java as simulated in a high-resolution ocean general circulation model. *Journal of Geophysical Research: Oceans*, 111, C12015. https://doi.org/10.1029/2006JC003486

Kalnay, E., Kanamitsu, M., Kistler, R., Collins, W., Deaven, D., Gandin, L., Iredell, M., Saha, et al. (1996). NCEP/NCAR 40-year reanalysis project. *Bulletin of the American Meteorological Society*, 77(3), 437–471.

Kämpf, J., & Kavi, A. (2019). SST variability in the eastern intertropical Indian Ocean – On the search for trigger mechanisms of IOD events. *Deep Sea Research. Part II*, 166, 64-74, doi:10.1016/j.dsr2.2018.11.010

Kang, S., Im, E. & Eltahir, E. A. B. (2019). Future climate change enhances rainfall seasonality in a regional model of western Maritime Continent. *Climate Dynamics*, 52, 747–764. https://doi.org/10.1007/s00382-018-4164-9

Kido, S., & Tozuka, T. (2017). Salinity variability associated with the positive Indian Ocean Dipole and its impact on the upper ocean temperature. *Journal of Climate*, 30(19), 7885–7907. https://doi.org/10.1175/JCLI-D-17-0133.1

Lau, K.-M., & Chang, P. H. (1986). Aspects of the 40–50 day oscillation during the northern summer as inferred from outgoing longwave radiation. *Monthly Weather Review*, 114, 1354–1367.

Lawrence, D. M., & P. J. Webster (2002). The boreal summer intraseasonal oscillation: Relationship between northward and eastward movement of convection, *Journal of Atmospheric Science*, 59, 1593–1606.

Liebmann, B., & Smith, C. A. (1996). Description of a complete (interpolated) outgoing longwave radiation dataset. *Bulletin of the American Meteorological Society*, 77(6), 1275–1277.

Lukas R., & Lindstrom E. (1991). The mixed layer of the western equatorial Pacific Ocean. *Journal of Geophysical Research: Oceans*, 96, 3343–3357.

Madden, R. A., & Julian, P. R. (1994). Observations of the 40-50-day tropical oscillation—A review. *Monthly Weather Review*, 122(5), 814–837.

Masumoto, Y., Sasaki, H., Kagimoto, T., Komori, N., Ishida, A., Sasai, Y., Miyama, T., Motoi, T., et al. (2004). A fifty-year eddy-resolving simulation of the world ocean: Preliminary outcomes of OFES (OGCM for the Earth Simulator). *Journal of Earth Simulator*, 1, 35–56.

Matsuyama, M., Senjyu, T., Natih N. N. M. (1996). Oceanographic conditions in Pelabuhanratu Bay, west Java. *La mer*, 34, 283–291.

Mori, S., Hamada, J.-I., Tauhid, Y. I., Yamanaka, M. D., Okamoto, N., Murata, F., Sakurai, N., Hashiguchi, H., Sribimawati, T. (2004). Diurnal land-sea rainfall peak migration over Sumatora Island, Indonesian maritime continent, observed by TRMM satellite and intensive rawinsonde soundings. *Monthly Weather Review* 132(8), 2021–2039.

Moteki, Q., Katsumata, M., Yoneyama, K, Ando, K., & Hasegawa, T. (2018). Drastic thickening of the barrier layer off the western coast of Sumatra due to the Madden-Julian oscillation passage during the Pre-Years of the Maritime Continent campaign. *Progress in Earth and Planetary Science*, 5, doi: 10.1186/s40645-018-0190-9

Murtugudde, R., McCreary, J. P., & Busalacchi, A. J. (2000). Oceanic processes associated with anomalous events in the Indian Ocean with relevance to 1997-1998. *Journal of Geophysical Research: Oceans*, 105(C2), 3295– 3306. https://doi.org/10.1029/1999JC900294

Ningsih, N. S., Rakhmaputeri, N., & Harto, A. B. (2013). Upwelling variability along the southern coast of Bali and in Nusa Tenggara waters. *Ocean Science Journal*, 48(1), 49–57.

Nguyen, P., E.J. Shearer, H. Tran, M. Ombadi, N. Hayatbini, T. Palacios, P. Huynh, G. Updegraff, K. Hsu, B. Kuligowski, W.S. Logan, & S. Sorooshian, The CHRS Data Portal, an easily accessible public repository for PERSIANN global satellite precipitation data, *Nature Scientific Data*, Vol. 6, Article 180296, 2019. doi: https://doi.org/10.1038/sdata.2018.296

Qu, T., & Meyers, G. (2005). Seasonal variation of barrier layer in the southeastern tropical Indian Ocean. *Journal of Geophysical Research: Oceans*, 110, C11003. https://doi.org/10.1029/2004JC002816

Reynolds, R. W., Smith, T. M., Liu, C., Chelton, D. B., Casey, K. S., & Schlax, M. G. (2007). Daily high-resolution-blended analyses for Sea Surface Temperature. *Journal of Climate*, 20, 5473–5496. https://doi.org/10.1175/2007JCLI1824.1

Saji, N. H., Goswami, B. N., Vinayachandran, P. N., & Yamagata, T. (1999). A dipole mode in the tropical Indian Ocean. *Nature*, 401, 360– 363.

Sprintall J., & Tomczak M. (1992). Evidence of the barrier layer in the surface layer of the tropics. *Journal of Geophysical Research: Oceans* 97(C5):7305–7316

Susanto, R. D., Gordon, A. L., & Zheng, Q. (2001). Upwelling along the coasts of Java and Sumatra and its relation to ENSO. *Geophysical Research Letters*, 28, 1599–1602.

Susanto, R. D., & J. Marra (2005). Effects of the 1997/98 El Niño on Chlorophyll a variability along the southern coasts of Java and Sumatra, *Oceanography*, 18(4), 124–127, doi:10.5670/oceanog.2005.13.

Susanto, R.D., Wei, Z., Adi, T. R., Zheng, Q., Fang, G., Fan, B., Supangat, A., Agustiadi, T. et al. (2016). Oceanography surrounding Krakatau Volcano in the Sunda Strait, Indonesia. *Oceanography* 29(2):264–272, http://dx.doi.org/10.5670/oceanog.2016.31

Tozer, B, Sandwell, D. T., Smith, W. H. F., Olson, C., Beale, J. R., & Wessel, P. (2019). Global bathymetry and topography at 15 arc sec: SRTM15+. *Earth and Space Science*. 6. https://doi.org/10.1029/2019EA000658

Webster, P. J., Moore, A. M., Loschnigg, J. P., & Leben, R. R. (1999). Coupled ocean-atmosphere dynamics in the Indian Ocean during 1997–98. *Nature*, 401 (6751), 356–360. https://doi.org/10.1038/43848

Wheeler, M., & Hendon, H. H. (2004). An all-season real-time multivariate MJO index: Development of an index for monitoring and prediction. *Monthly Weather Review*, 132, 1917–1932.

Wyrtki, K. (1962). The upwelling in the region between Java and Australia during the south-east monsoon. *Australian Journal of Marine and Freshwater Research*, 13, 217–225.

Yoshida, K. (1955). Coastal upwelling off the California coast. *Records of Oceanographic Works in Japan*, 15, 1-13.

Zhang, C. (2005). Madden-Julian Oscillation. *Review of Geophysics*, 43, RG2003, doi:10.1029/2004RG000158